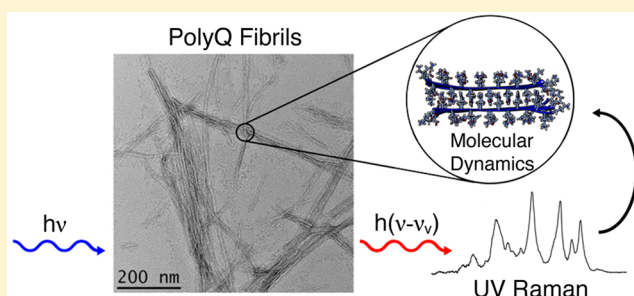


Polyglutamine Fibrils: New Insights into Antiparallel β -Sheet Conformational Preference and Side Chain Structure

David Punihaole,[†] Riley J. Workman,[‡] Zhenmin Hong,[†] Jeffrey D. Madura,^{*,‡} and Sanford A. Asher^{*,†}[†]Department of Chemistry, University of Pittsburgh, Pittsburgh, Pennsylvania 15260, United States[‡]Department of Chemistry and Biochemistry, Center for Computational Sciences, Duquesne University, Pittsburgh, Pennsylvania 15282, United States

Supporting Information

ABSTRACT: Understanding the structure of polyglutamine (polyQ) amyloid-like fibril aggregates is crucial to gaining insights into the etiology of at least ten neurodegenerative disorders, including Huntington's disease. Here, we determine the structure of D₂Q₁₀K₂ (Q10) fibrils using ultraviolet resonance Raman (UVRR) spectroscopy and molecular dynamics (MD). Using UVRR, we determine the fibril peptide backbone Ψ and glutamine (Gln) side chain χ_3 dihedral angles. We find that most of the fibril peptide bonds adopt antiparallel β -sheet conformations; however, a small population of peptide bonds exist in parallel β -sheet structures. Using MD, we simulate three different potential fibril structural models that consist of either β -strands or β -hairpins. Comparing the experimentally measured Ψ and χ_3 angle distributions to those obtained from the MD simulated models, we conclude that the basic structural motif of Q10 fibrils is an extended β -strand structure. Importantly, we determine from our MD simulations that Q10 fibril antiparallel β -sheets are thermodynamically more stable than parallel β -sheets. This accounts for why polyQ fibrils preferentially adopt antiparallel β -sheet conformations instead of in-register parallel β -sheets like most amyloidogenic peptides. In addition, we directly determine, for the first time, the structures of Gln side chains. Our structural data give new insights into the role that the Gln side chains play in the stabilization of polyQ fibrils. Finally, our work demonstrates the synergistic power and utility of combining UVRR measurements and MD modeling to determine the structure of amyloid-like fibrils.



INTRODUCTION

There are at least ten neurodegenerative disorders, including Huntington's disease, that are associated with mutational expansions in genomic CAG codon repeats.¹ These expansions increase the length of polyQ repeats in proteins. The increase in the repeat length of polyQ segments greatly enhances protein misfolding and aggregation. Although the exact mechanism of neurotoxicity is still heavily debated, the pathological hallmark of all CAG repeat diseases is the formation of large neuronal inclusions composed of polyQ-rich aggregates.^{2–4} Given their potential role in neurotoxicity, it is therefore crucial to understand the structure of polyQ-rich aggregates.

Numerous structures have been proposed for polyQ fibrils based on the results of many different biophysical methods. For example, X-ray diffraction studies indicate that polyQ fibrils of various Gln repeat lengths all show similar X-ray diffraction patterns. Despite this, these studies assign very different structures from surprisingly similar X-ray data, including "polar-zippers,"⁵ β -helices,⁶ and canonical β -sheet structures.^{7,8}

More recent structural studies of polyQ fibril aggregates use solid-state NMR. One of these studies⁹ concludes that the basic structural motif of polyQ fibrils prepared from pathologically relevant peptides is a " β -arc," similar to that of A β .^{10,11} The β -

arc model has been challenged by other solid-state NMR and biochemical studies,^{12,13} which alternatively suggest that polyQ fibrils are composed of extended β -strands that contain reverse hairpin turns.

In recent years, several molecular dynamics (MD) approaches have also been used to investigate the structural properties of polyQ-rich fibrils. The bulk of these computational studies focus mainly on the kinetic or thermodynamic stability of different fibril structures.^{14–17} However, these MD studies are conducted independently of experimental studies. Thus, there is little *direct* validation of the computational results against experimental data.

The lack of consensus regarding the structure of polyQ fibrils underscores the need for new and incisive biophysical methods that can *quantitatively* discriminate between the many proposed models. A fundamental factor in understanding polyQ fibrils is determining the structures and hydrogen bonding environments of the Gln side chains, which are thought to play an important role in stabilizing the aggregates. Another important structural property to understand is the propensity of polyQ

Received: November 20, 2015

Revised: March 4, 2016

Published: March 5, 2016

fibrils to adopt antiparallel β -sheets instead of in-register parallel β -sheets, like most amyloidogenic peptides and prions.

Ultraviolet resonance Raman (UVRR) spectroscopy is a powerful biophysical tool for studying the conformational ensembles and aggregation dynamics of amyloidogenic peptides.^{18–23} An advantage of UVRR is that quantitative information can be obtained quickly, under dilute conditions, and without the need for extensive or complex isotopic labeling of peptides and proteins.²⁴ In recent years, numerous UVRR spectroscopic markers have been discovered. Some of these markers are sensitive to the Ramachandran Ψ angles of the peptide bonds,^{25,26} while others are sensitive to the dihedral angles of amino acid side chains,^{27–29} including Asn and Gln.³⁰ Other marker bands are sensitive to the hydrogen bonding and the dielectric environments of peptide bonds and side chains.^{28,31–35}

We can combine structural information obtained from interpreting these spectral markers with results from MD simulations to determine the structure of polyQ and other amyloid-like fibrils. An elegant example of this approach was recently published by Buchanan et al.,³⁶ who combined two-dimensional infrared (2D IR) spectroscopy with MD simulations to determine the structure of $K_2Q_{24}K_2W$ fibrils. They concluded that $K_2Q_{24}K_2W$ fibrils adopt an antiparallel β -sheet structure that contains β -turns, but not β -arc structures, after comparing their experimental Amide I spectra with those calculated from simulated models.

In this work, we synergistically couple UVRR and MD to determine the structures of polyQ amyloid-like fibrils prepared from the model peptide $D_2Q_{10}K_2$ (Q10). Xiong et al.³⁷ previously showed that this peptide can exist in two distinct solution-state conformations, a putative β -hairpin-like structure (called NDQ10) and a PPII-like structure (called DQ10). We show that both NDQ10 and DQ10 peptide solutions can aggregate into amyloid-like fibrils. We use UVRR to measure the Ramachandran Ψ angle distributions of the NDQ10 and DQ10 fibril peptide bonds, as well as their Gln χ_3 ($O_{\epsilon 1}-C_{\delta}-C_{\gamma}-C_{\beta}$) side chain dihedral angles.

To determine the structure of NDQ10 and DQ10 fibrils, we compare our experimentally determined Ψ and χ_3 angle distributions to those obtained from three MD simulated fibril models (Figure 1). On the basis of these comparisons, we find that Q10 fibrils consist of extended β -strands that predominantly assemble into antiparallel β -sheets; however, small populations of Q10 peptide bonds are in parallel β -sheet structures. From our MD simulations, we determine that polyQ fibrils in antiparallel β -sheets are lower in free energy compared to parallel β -sheets. This energetic preference appears unique for polyQ fibrils compared to typical amyloid-like fibrils, where in-register parallel β -sheets are thought to be at lower energy.³⁸ Finally, our χ_3 dihedral angle measurements and MD simulations of Q10 fibrils leads us to propose a new model for the structure of Gln side chains in polyQ fibrils.

EXPERIMENTAL SECTION

Materials. The 14-residue peptide, $D_2Q_{10}K_2$ (Q10), was purchased from AnaSpec Inc. at $\geq 95\%$ purity. Trifluoroacetic acid (TFA) was purchased from Acros at 99.5% purity, and 1,1,1,3,3,3-hexafluoro-2-propanol (HFIP) was obtained from Fluka at $\geq 99\%$ purity. HPLC-grade H_2O was purchased from Fisher Scientific, and D_2O (99.9 atom % D) was purchased from Cambridge Isotope Laboratories, Inc. NaOD (40 wt %

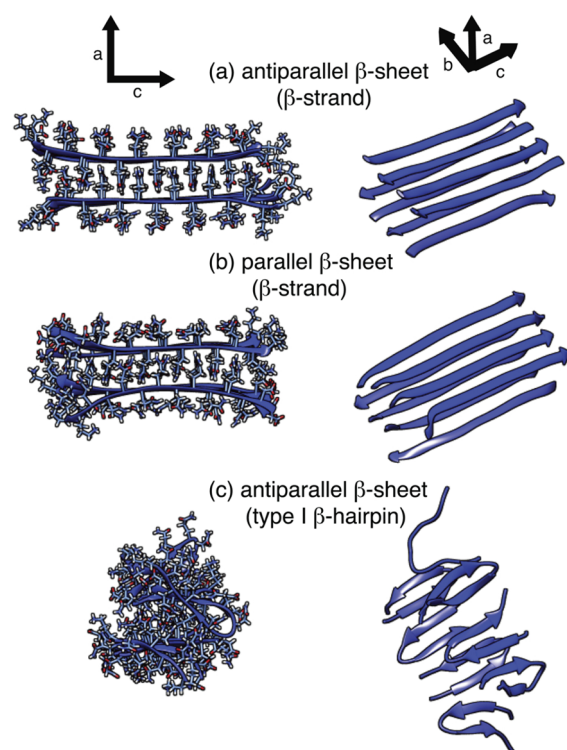


Figure 1. MD simulated structures of model Q10 fibril systems in (a) a β -strand configuration with an antiparallel β -sheet architecture, (b) a β -strand configuration with a parallel β -sheet architecture, and (c) a Type I β -hairpin configuration with an antiparallel β -sheet architecture. The a, b, and c axes refer to the inter-sheet, inter-strand, and intra-chain dimensions, respectively, of the fibril models.

solution in D_2O , 99+ atom % D) and L-glutamine (99% purity) was purchased from Sigma-Aldrich.

Sample Preparation. NDQ10 peptide solutions were prepared by dissolving Q10 directly in H_2O or D_2O . DQ10 solutions were prepared using a standard protocol based on a method developed by Wetzel and Chen.³⁹ Briefly, DQ10 samples were prepared by suspending the lyophilized Q10 peptide powder received from Anaspec Inc. in a 1:1 (v/v) mixture of TFA and HFIP. The samples were sonicated for 20 min and incubated at room temperature for 2 h. The solvents were evaporated under a gentle stream of dry N_2 gas for 1 h. The peptide film was dissolved in H_2O or D_2O and ultracentrifuged at 627 000g for 30 min at 4 °C. The top 2/3 of the solution was decanted and used for the aggregation reaction.

Fibril aggregates were prepared by initially dissolving NDQ10 and DQ10 prepared peptides in H_2O or D_2O at 5 $mg \cdot mL^{-1}$ concentrations and incubating the samples at 60 °C in vials sealed with Teflon tape. Solutions were titrated to pH 7 (pD 8) using NaOH (NaOD) solutions. After incubation for 6 days, aggregates were harvested via centrifugation, and the pellets were resuspended in 120 μL of H_2O or D_2O . For the hydrogen–deuterium exchange (HX) experiments, harvested aggregates prepared in H_2O (D_2O) were washed in 500 μL of D_2O (H_2O), centrifuged, and the supernatant removed. The pellets were resuspended in 120 μL of D_2O (H_2O) and incubated for 3 h at room temperature in sealed vials.

Transmission Electron Microscopy (TEM). A 10 μL aliquot of aggregate solution was placed onto a freshly glow-discharged carbon-coated grid for 2 min before being blotted

dry with filter paper. Samples were stained with 10 μL of 1% (w/v) uranyl acetate for 2 min, and the excess stain was removed by blotting the grid. Grids were imaged using a Tenai F20 electron microscope (FEI Co.) operating at 200 kV and equipped with a 4k \times 4k CCD camera (Gatan).

X-ray Diffraction of Fibril Films. Aggregates prepared from the NDQ10 peptide solutions were placed into the wide end of a 0.7 mm diameter quartz X-ray capillary tube (Charles Supper Company). The wide end of the tube was sealed with melted beeswax, and the thin end of the tube was left open for drying. DQ10 aggregates were mounted on the broken end of a quartz capillary tube and dried. Aggregate samples were placed on the end of a goniometer head and centered in the X-ray beam path. X-ray diffraction patterns were collected using a Bruker X8 Prospector Ultra instrument with a Copper microfocus tube ($\lambda = 1.54178 \text{ \AA}$) and equipped with an Apex II CCD detector. All data were collected at room temperature with exposure times of 60 min.

UVR Spectroscopy. The UVR instrumentation used is described in detail by Bykov et al.⁴⁰ Briefly, $\sim 204 \text{ nm}$ light was obtained by mixing the third harmonic with the 816 nm fundamental generated by a tunable Ti:sapphire system (Photonics Industries) operating at 1 kHz. An Indigo S tunable Ti:sapphire system (Positive Light), operating at 5 kHz, generated $\sim 197 \text{ nm}$ light by mixing the third harmonic with the $\sim 788 \text{ nm}$ fundamental. For fibrils measured in solution, the laser light was focused onto a spinning Suprasil quartz NMR tube containing the sample. The average laser power at the sample ranged from ~ 0.4 – 0.5 mW . A $\sim 165^\circ$ backscattering geometry was used. The total acquisition time to collect spectra was only $\sim 10 \text{ min}$. The scattered light was imaged into a home-built subtractive double monochromator and detected with a liquid N_2 cooled, back-thinned Spec-10:400B CCD camera (Princeton Instruments) with a Lumogen E coating. The spectrometer resolution was $\sim 5 \text{ cm}^{-1}$ at the excitation wavelengths used. A description of how the spectra were processed is in the [Supporting Information](#).

COMPUTATIONAL SECTION

We considered three model fibril systems, as shown in [Figure 1](#). These systems are composed of eight Q10 peptides that are assembled into parallel and antiparallel β -sheets. The two β -sheets were oriented parallel to each other, but rotated by 180° , to maximize attractive electrostatic interactions between terminal Asp and Lys residues. Models *a* and *b* were constructed using canonical β -sheet Ramachandran dihedral angles.⁴¹ In the case of model *a*, we used canonical antiparallel β -sheet (Φ, Ψ) angles of ($-140^\circ, 135^\circ$). For model *b*, we used canonical parallel β -sheet (Φ, Ψ) angles of ($-120^\circ, 113^\circ$). Model *c* was constructed using β -hairpin geometries observed in metadynamics simulations (data not shown). These model fibrils were constructed using the Molecular Operating Environment (MOE 2013.10) software suite⁴¹ and were solvated in a water box. Files containing the initial structure coordinates used in the MD simulations, as well as the NAMD configuration templates, are available for download in the [Supporting Information](#).

After the models were constructed, the solvated fibril systems were energy minimized for 10 000 steps using the conjugate gradient method and then equilibrated for 50 ps. During equilibration, the fibril atoms were initially restrained by harmonic potentials. After the water molecules around the restrained fibrils were relaxed, the water molecules and peptide

side chains were then energy-minimized for 10 000 steps. This was followed by 100 ps of equilibration, in which the peptide backbone atoms were restrained. The model fibril systems were then equilibrated for an additional 50 ns without restraints. All fibril models retained structural integrity throughout the energy minimization and equilibration. The fibril models were simulated using classical MD for 200 ns.

MD simulations were performed with the NAMD software package (version 2.10).⁴² The potential energies were calculated with the CHARMM22/CMAP force field.⁴³ This force field was chosen for its torsional energy corrections intended to decrease α -helix bias and stabilize β -strand secondary structures. Other force fields, such as Amber99ffsb,⁴⁴ also implement these corrections; however, CHARMM22/CMAP⁴³ was selected because of its reported accuracy in describing α -helix, β -sheet, and disordered structures.⁴⁵ The fibril models were solvated using the solvate module of VMD 1.9.1,⁴⁶ resulting in a periodic box of 5000 water molecules with dimensions of $70 \times 50 \times 50 \text{ \AA}^3$ for a total system size of 17 189 atoms. The TIP3P water model⁴⁷ was employed in all simulations, and the particle mesh Ewald algorithm⁴⁸ was used with a grid spacing of 1.0 \AA to calculate full system electrostatics. An integration time step of 2 fs was employed. Simulations were performed under the NPT ensemble, with a Langevin thermostat and piston utilized to regulate the temperature of 300 K and pressure of 1.01325 bar, respectively. The pair interaction cutoff was 12.0 \AA , and the switch distance was 10.0 \AA .

Simulation analysis was performed using VMD 1.9.1 and Tcl scripting. The Ψ and χ_3 dihedral angles were obtained for all Gln residues with a Tcl script in VMD. The χ_3 dihedral angles were obtained from Gln side chains that were not significantly solvent exposed, so as to best simulate the interior of a fibril environment. The extent of β -sheet dissociation was determined qualitatively by viewing the trajectories and monitoring the dissociation of peptides. This qualitative analysis was also paired with a quantitative root-mean-square deviation (RMSD) metric (see the [Supporting Information](#) for details).

The Gibbs free energy difference between the [Figure 1](#) model *a* antiparallel and model *b* parallel β -strand fibril structures was calculated using a Python implementation of the Bennett acceptance ratio method, called Pymbar.⁴⁹ Potential energies were obtained from the NAMD log output files and used as inputs for Pymbar via a Python script that can be found in the [Supporting Information](#).

Hydrogen bonding analysis on models *a* and *b* (from [Figure 1](#)) was also done by using VMD 1.9.1. Hydrogen bond contacts were defined by a heavy atom ($\text{N}\cdots\text{O}$) distance of $<3.0 \text{ \AA}$ and a $\text{N-H}\cdots\text{O}$ angle between -30° and 30° . The number of peptide backbone–backbone, backbone–side chain, side chain–side chain, and peptide–water hydrogen bonds were calculated for models *a* and *b* over the course of the entire trajectory. The data for each hydrogen bond category was binned for each model and plotted with the statistical computing package R (see the [Supporting Information](#)).

RESULTS AND DISCUSSION

Q10 Forms Amyloid-like Fibril Aggregates. [Figure 2a,b](#) shows the TEM images of NDQ10 and DQ10 aggregates. The TEM images of both NDQ10 and DQ10 aggregates resemble those of amyloid-like fibrils and exhibit morphologies similar to those of polyQ peptides with larger, more pathologically

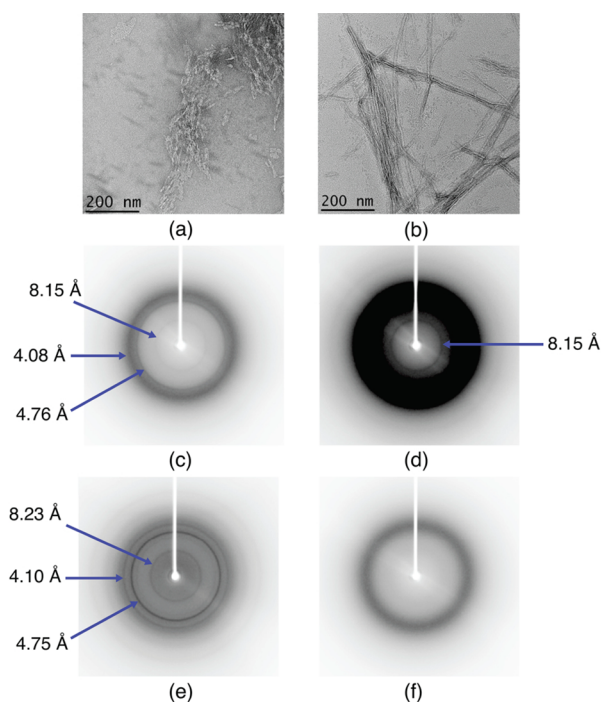


Figure 2. TEM micrographs and X-ray diffraction patterns of NDQ10 and DQ10 fibril aggregates. TEM images of (a) NDQ10 and (b) DQ10 fibrils. The scale bars represent 200 nm. X-ray diffraction pattern of (c, d) NDQ10 fibril films, and (e) DQ10 fibril films, and (f) the quartz capillary tube. The patterns shown in panels c and d are the same except for the contrast settings, which have been set in panel d to highlight the weak reflection at ~ 8.2 Å.

relevant Gln repeat lengths.⁵⁰ NDQ10 aggregates (Figure 2a) cluster into dense meshworks composed of small, thin fibrils, while DQ10 (Figure 2b) forms long, ribbonlike fibrils.

We used X-ray diffraction to further characterize the fibril-like nature of NDQ10 and DQ10 aggregates. Oriented amyloid fibril films exhibit a characteristic diffraction pattern with a “meridional reflection” at ~ 4.8 Å and an “equatorial reflection” at ~ 10 – 12 Å. This diffraction pattern is the hallmark of cross- β structures, wherein constituent β -strands orient perpendicular to the long axis of the fibril. The meridional reflection is indicative of the spacing between β -strands, and the equatorial reflection is indicative of the spacing between β -sheets in the fibrils.

Figure 2c–e shows the “powder-like” diffraction patterns of unoriented NDQ10 and DQ10 aggregate films. There are reflections at ~ 4.1 , ~ 4.8 , and ~ 8.2 Å observed in the diffraction patterns of NDQ10 and DQ10. Similar reflections have been observed in larger sequences of polyQ fibrils in previous studies.^{7,8} On the basis of these previous studies, we assign the prominent ~ 4.8 Å reflection to the repeat distance between neighboring β -strands within the fibril β -sheets. The weaker ~ 8.2 Å reflection is assigned to the inter- β -sheet stacking repeat distance.

The equatorial reflections of most amyloid-like fibrils are very diffuse, which indicates limited ordering and disordered growth in the inter- β -sheet dimension.⁵¹ In contrast, polyQ fibrils usually show very sharp reflections between ~ 8 and 9 Å. We observe reflections at ~ 8.15 and ~ 8.23 Å in NDQ10 and DQ10, respectively. A higher-order reflection occurs at ~ 4.1 Å for both NDQ10 and DQ10. The presence of these higher orders and the narrowness of the ~ 8.2 Å reflections suggests

that there is long-range ordering in the inter- β -sheet dimension of polyQ fibrils.^{7,8} As noted by Atkins and Sikorski,⁷ this long-range ordering presumably arises from the tight interdigitation of the Gln side chains from neighboring sheets. In addition, there is strong interamide hydrogen bonding interactions between neighboring side chains of the same β -sheet.

UVRR of Polyglutamine Fibrils in H₂O. We utilized UVRR to investigate the molecular structure of NDQ10 and DQ10 fibrils in solution. The ~ 197 and ~ 204 nm excited UVRR spectra of NDQ10 and DQ10 fibrils are shown in Figure 3. Raman excitation at ~ 200 nm occurs within the NV₁ electronic transitions of secondary amide peptide bonds and to the long wavelength side on the NV₁ transitions of Gln side chain primary amide groups.^{37,52} Thus, the ~ 200 nm excitation UVRR spectra of polyQ peptides are dominated mainly by resonance-enhanced bands that derive from primary and secondary amide (Am) vibrations, which we label with the superscripts ^P and ^S, respectively.

Assignment of Gln Side Chain Bands. The main difference between the ~ 197 and ~ 204 nm excited UVRR spectra are the relative intensities of the primary (side chain) and secondary (peptide bond) amide bands. We previously showed that excitation at ~ 197 nm enhances primary amide UVRR bands significantly more than ~ 204 nm excitation.³⁷ As a result, primary amide vibrations can be highlighted by calculating the difference spectrum between the ~ 197 and ~ 204 nm UVRR spectra.

Figure 3 shows that the 197–204 nm difference spectra highlights the primary amide bands of the Gln side chains in NDQ10 and DQ10 fibrils. The AmI^P (predominately a C_δ=O_{ε1} stretching vibration) and the AmII^P (mainly N_{ε2}H₂ scissoring) bands are located at ~ 1660 and ~ 1615 cm⁻¹, respectively, for both NDQ10 and DQ10 fibrils. In addition, both NDQ10 and DQ10 show a band at ~ 1100 cm⁻¹ that derives from an in-phase combination of C_δ-N_{ε2} stretching and N_{ε2}H₂ rocking motions. As discussed in detail below, this vibration, which we call the AmIII^P, is sensitive to the structure of the Gln side chains.

The primary amide band frequencies and Raman cross sections are very sensitive to the hydrogen bonding and the local dielectric environment of Gln side chains.³⁵ For example, the AmI^P band frequency is diagnostic of C_δ=O_{ε1} hydrogen bonding. The AmII^P band frequency reports on hydrogen bonding of the N_{ε2}H₂ group. Compared to monomeric Gln in water,³⁰ the NDQ10 and DQ10 fibril AmI^P bands are downshifted by ~ 20 cm⁻¹, while the AmII^P bands are downshifted by ~ 7 cm⁻¹. These frequency downshifts indicate that the interamide hydrogen bonding within the fibrils is much stronger than the amide–H₂O hydrogen bonding that occurs for monomeric Gln. In addition, the NDQ10 and DQ10 fibril AmI^P and AmII^P bands show very narrow line widths, similar to those seen in UVRR spectra of Gln crystals,³⁰ which indicates that the primary amide groups are in very well-defined hydrogen bonding states.

The most noticeable difference between the NDQ10 and DQ10 fibril 197–204 nm difference spectra occur for strong bands located between ~ 1400 and 1500 cm⁻¹. A band located at ~ 1415 cm⁻¹ in NDQ10 fibrils upshifts ~ 15 cm⁻¹ in DQ10 fibrils. This band derives from a complex vibration that contains CH₂ wagging, C–C stretching, CH₂ scissoring, and C_δ-N_{ε2} stretching motions. Based on our previous work,³⁵ an upshifted CH₂ wagging band signals that the Gln side chains are in an environment of higher dielectric constant. Thus, we conclude

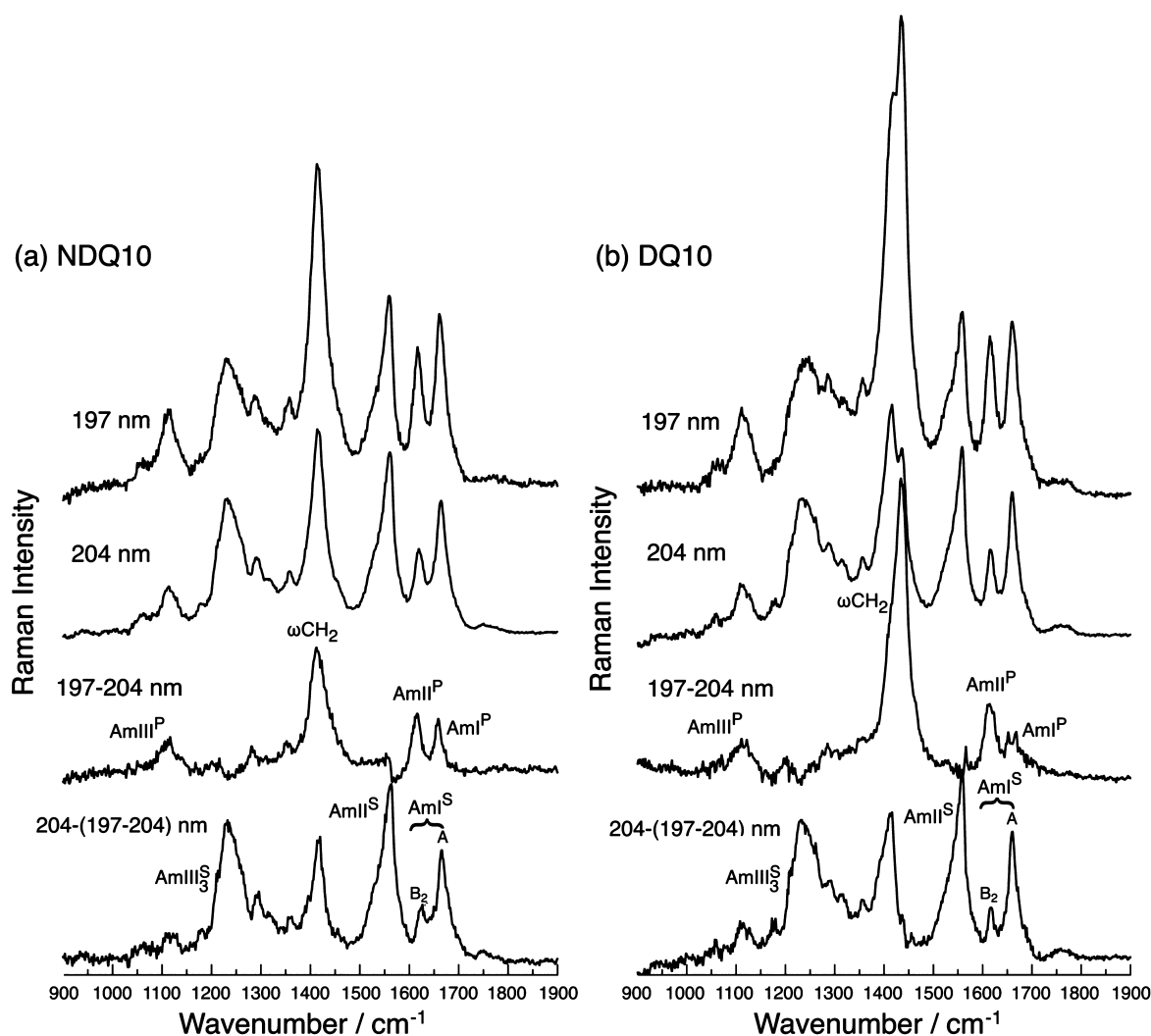


Figure 3. UVRR spectra (197 and 204 nm excitation) of (a) NDQ10 and (b) DQ10 fibrils prepared in H₂O. The spectra were measured on precipitates that were resuspended in H₂O.

that the DQ10 Gln side chain methylene groups are in a higher dielectric constant environment than are those of NDQ10. This presumably correlates with the ~ 0.8 Å larger inter- β -sheet spacing for DQ10 fibrils compared to NDQ10 fibrils (Figure 2c–e). The larger inter-sheet spacing allows solvating water molecules to penetrate deeper into DQ10 fibrils, increasing the local dielectric constant. This hypothesis is supported by the results shown in Figure S3, wherein the CH₂ wagging band downshifts to ~ 1415 and ~ 1407 cm⁻¹ in dried DQ10 and NDQ10 fibril films, respectively.

Assignment of Peptide Backbone Bands. We subtracted the 197–204 nm difference spectra from the 204 nm excited UVRR spectra to reveal the peptide bond secondary amide bands. The AmI^S (mainly peptide backbone C=O stretching) appears as two bands (labeled as AmI_A^S and AmI_{B2}^S) in the spectra of both NDQ10 and DQ10 fibrils. This “excitonic splitting” is diagnostic of β -sheet structures and derives from through-space transition dipole coupling between the AmI^S oscillators. The Raman spectral AmI^S splitting patterns of antiparallel and parallel β -sheets are similar. Thus, it is usually difficult to discriminate between these two structures using this band alone.^{53,54}

The intense, high-frequency AmI^S band (labeled as the AmI_A^S) appears at ~ 1665 and ~ 1660 cm⁻¹ in NDQ10 and

DQ10 fibrils, respectively. The less intense, low-frequency AmI^S band (AmI_{B2}^S) appears at ~ 1620 cm⁻¹ in NDQ10 and at ~ 1615 cm⁻¹ in DQ10. These ~ 5 cm⁻¹ decreases in the AmI^S mode frequencies suggest slightly stronger peptide backbone C=O hydrogen bonding between β -strands in DQ10 fibrils than in NDQ10 fibrils.⁵⁵ We are, however, aware that the Raman and IR AmI^S bands can also be impacted by β -sheet twisting and stacking, as well as the registry of the β -strands, as described in detail by Keiderling and co-workers.⁵³ Thus, these AmI^S frequency differences between NDQ10 and DQ10 could also signal subtle differences in the twisting and stacking of the fibril β -sheets. We are continuing to examine these issues.

The extended AmIII^S UVRR spectral region between 1200 and 1350 cm⁻¹ is generally considered to be the most structurally informative.²⁴ This region in polyQ peptides is complicated because of the overlap of bands from Gln side chain CH₂ twisting and wagging modes that occur between ~ 1280 and 1350 cm⁻¹. In addition, the AmIII^S region consists of three sub-bands (called the AmIII₁^S, AmIII₂^S, and AmIII₃^S), which derive from vibrations that are composed of in-phase combinations of peptide bond N–H in-plane bending and C–N stretching motions.

Mikhonin et al.⁵⁶ previously assigned the AmIII₁^S, AmIII₂^S, and AmIII₃^S bands in detail. In NDQ10 and DQ10 fibrils, the AmIII₁^S

occurs at $\sim 1315\text{ cm}^{-1}$, while the $\text{AmIII}_2^{\text{S}}$ occurs at $\sim 1290\text{ cm}^{-1}$, and the $\text{AmIII}_3^{\text{S}}$ occurs between ~ 1200 and 1280 cm^{-1} . Both NDQ10 and DQ10 show peaks at $\sim 1230\text{ cm}^{-1}$ and low-frequency shoulders at $\sim 1210\text{ cm}^{-1}$. As discussed in detail below, the $\text{AmIII}_3^{\text{S}}$ band frequency is sensitive to the Ramachandran Ψ dihedral angle and thus can be used to obtain quantitative information on the secondary structure of polyQ fibrils.

UVRR of Polyglutamine Fibrils in D_2O . Figure 4 shows the UVRR spectra of NDQ10 and DQ10 fibrils prepared and

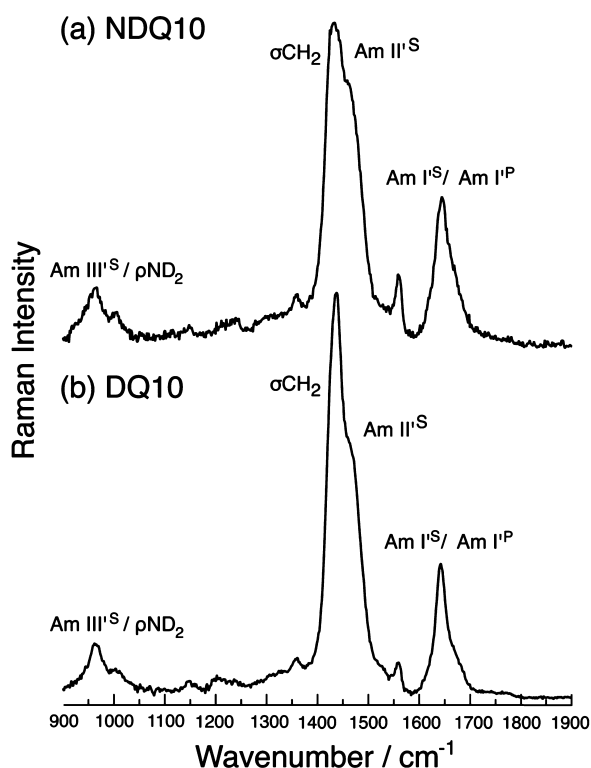


Figure 4. UVRR spectra (204 nm excitation) of (a) NDQ10 and (b) DQ10 fibrils prepared in D_2O . The spectra were measured on precipitates that were resuspended in D_2O .

measured in D_2O . Deuteration of the polyQ peptide backbone N–H and primary amide side chain $\text{N}_{\text{e}2}\text{H}_2$ groups leads to significant spectral changes. Upon N-deuteration, the AmI^{S} downshifts to $\sim 1640\text{ cm}^{-1}$ (AmI^{S}) and overlaps the AmI^{P} . In the case of the AmIII^{S} mode, deuteration decouples N–H in-plane bending from C–N stretching.⁵⁶ This leaves a weak AmIII^{S} band (mainly N–D in-plane bending) in the ~ 950 – 1050 cm^{-1} region. The AmIII^{S} region also contains bands that derive from side chain $\text{N}_{\text{e}2}\text{D}_2$ rocking modes.⁵⁶ The loss of the AmIII^{S} band reveals the presence of several weak bands between ~ 1300 and 1400 cm^{-1} , which derive mainly from side chain CH_2 and peptide backbone C–H deformation modes.

Hydrogen–Deuterium Exchange of Polyglutamine Fibrils. A comparison of Figures 3 and 4 shows that UVRR can be employed to differentiate between N–H and N–D peptide bonds. Hydrogen–deuterium exchange can selectively probe solvent-exposed versus solvent-shielded peptide bonds in fibrils because the AmIII^{S} completely disappears upon N-deuteration.²⁰ For example, fibrils prepared in H_2O and subjected to HX in D_2O will show $\text{AmIII}_3^{\text{S}}$ bands that derive mainly from peptide bonds shielded from solvent, such as those

that are buried within the cross- β core. In contrast, fibrils prepared in D_2O that are subjected to HX in H_2O will show $\text{AmIII}_3^{\text{S}}$ bands that derive mainly from peptide bonds that are solvent accessible, generally because they are located on the aggregate surface or because they exist in exchangeable conformations such as “disordered” regions, turns, or loops.

UVRR Bands of Partially Deuterated Primary Amides. Extensive HX of polyQ fibrils may not completely deuterate the primary amide $\text{N}_{\text{e}2}\text{H}_2$ groups because the Gln side chains may be involved in extensive hydrogen bonding interactions. Based on Saito and co-workers’ normal mode analyses of acetamide,^{57,58} the partial deuteration of primary amides results in decoupling of N–H and N–D motions. As shown below, monodeuteration of primary amides can give rise to secondary amide-like vibrational modes! Thus, it is conceivable that monodeuterated Gln side chains can result in AmIII^{S} -like vibrations.

To investigate the potential presence of AmIII^{S} -like vibrations in monodeuterated primary amides, we measured the UVRR spectrum of Gln in a 50%/50% mixture of H_2O and D_2O . The spectrum, shown in Figure 5, was assigned with the

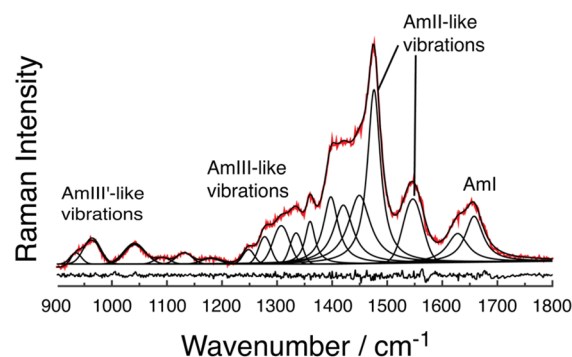
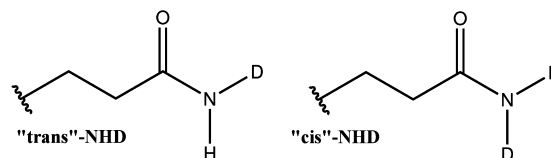


Figure 5. UVRR spectrum (204 nm excitation) of Gln measured in a 50% H_2O /50% D_2O mixture. The spectral contributions of solvent, as well as fully protonated and fully deuterated Gln, have been subtracted.

aid of DFT calculations (see the Supporting Information for details). We considered two geometrical isomers in calculating the vibrational normal modes of partially deuterated Gln, as shown in Scheme 1. The “trans-NHD” Gln species resembles

Scheme 1. Geometric Isomers of the Monodeuterated Primary Amide Group of Gln Side Chains



the trans-isomer configuration of the peptide bond and thus is expected to give rise to vibrations that resemble the canonical AmI^{S} , AmII^{S} , and AmIII^{S} vibrations of secondary amides.

We present a detailed assignment of the Figure 5 spectrum in the Supporting Information, as shown in Tables S1–S3. According to our normal mode analysis, we assign an AmI^{S} -like vibration to an $\sim 1660\text{ cm}^{-1}$ band and two AmII^{S} -like vibrations to bands located at ~ 1550 and $\sim 1475\text{ cm}^{-1}$. The DFT calculations also indicate that the ~ 1250 – 1400 cm^{-1} region contains four vibrations with significant C_{β} – $\text{N}_{\text{e}2}$ stretching

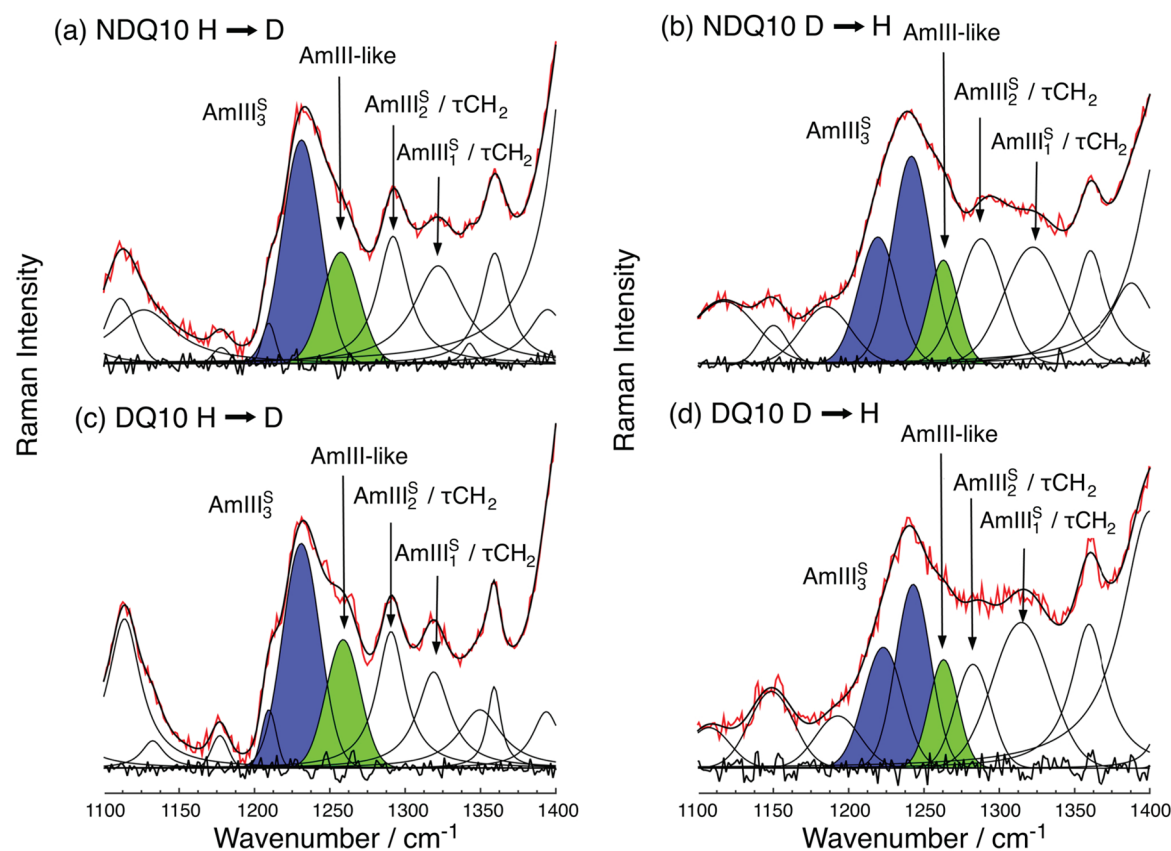


Figure 6. HX-UVRR spectra (204 nm excitation) of (a, b) NDQ10 and (c, d) DQ10 fibrils. For panels a and c, fibrils were prepared in H_2O and exchanged in D_2O . For panels b and d, fibrils were prepared in D_2O and exchanged in H_2O . The spectra were measured on precipitates that were resuspended in either H_2O or D_2O .

character. Two of these vibrations derive from the cis-NHD species of Gln and are assigned to the ~ 1335 and ~ 1280 cm^{-1} bands. The other two vibrations at ~ 1310 and ~ 1250 cm^{-1} derive from the trans-NHD species of Gln. These modes resemble AmIII^S-like vibrations because they contain a significant combination of NHD scissoring and $\text{C}_\delta\text{-N}_{\text{e}2}$ stretching motions.

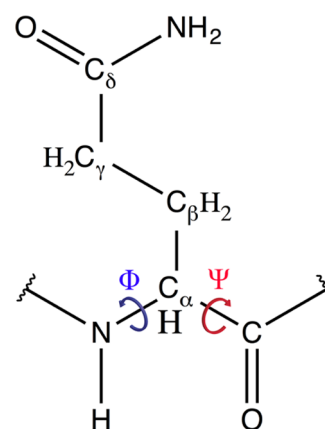
HX of NDQ10 and DQ10 Fibrils. Our normal mode analysis and band assignments of the Figure 5 Gln spectrum indicate that HX of polyQ fibrils can result in partially deuterated Gln side chains that give rise to AmIII^S-like vibrations. These AmIII^S-like bands appear in the high-frequency side of the AmIII^S region; however, they do not significantly overlap with that of the AmIII^S region of β -sheets, which occurs between ~ 1200 and 1240 cm^{-1} . Thus, we can straightforwardly assign the β -sheet AmIII^S bands of NDQ10 and DQ10 fibrils in the HX-UVRR spectra.

Figure 6 shows the curve-resolved AmIII^S region of the UVRR spectra of NDQ10 and DQ10 fibrils following HX. The spectra labeled as H \rightarrow D (D \rightarrow H) were measured from fibrils prepared in H_2O (D_2O) and subjected to HX in D_2O (H_2O). The bands shown in blue are assigned to true AmIII^S vibrations, while those shown in green are assigned to the AmIII^S-like vibrations that derive from partially deuterated primary amides. The H \rightarrow D spectra of NDQ10 and DQ10 fibrils show AmIII^S bands at ~ 1210 and ~ 1230 cm^{-1} . These bands upshift ~ 10 cm^{-1} in the D \rightarrow H spectra. As discussed in detail by Mikhonin et al.,²⁶ this peptide bond frequency upshift can result from an increased hydrogen bonding to water which does not involve any structural changes. Thus, we conclude that the Q10 fibril

exterior peptide bonds are more extensively hydrogen bonded to water than those in the fibril interior.

Ramachandran Ψ Angle Distributions. The AmIII^S band is the most conformationally sensitive secondary amide band because its frequency depends sinusoidally on the Ramachandran Ψ dihedral angle (see Scheme 2) of the peptide backbone.^{25,26} This sinusoidal dependence derives from the coupling of the $\text{C}_\alpha\text{-H}$ bending vibration with the N-H bending component of the AmIII^S vibration. For example, this coupling is strong for β -strand and PPII-like peptide bond angles, when the $\text{C}_\alpha\text{-H}$ and N-H groups are in an

Scheme 2. Depiction of Ramachandran Ψ and Φ Dihedral Angles in Polyglutamine Peptides



approximately cis-configuration. The strong coupling between N–H and C $_{\alpha}$ –H bending motions downshifts the AmIII $_3^S$ frequency. In contrast, for α -helical-like Ψ angles, the C $_{\alpha}$ –H and N–H groups are in a trans-configuration to each other, which results in the C $_{\alpha}$ –H and N–H bending motions decoupling. This decoupling results in the AmIII $_3^S$ band upshifting.

We utilized the structural sensitivity of the AmIII $_3^S$ band to determine Ramachandran Ψ dihedral angle distributions for the NDQ10 and DQ10 fibril peptide bonds (Figure 7). To do this,

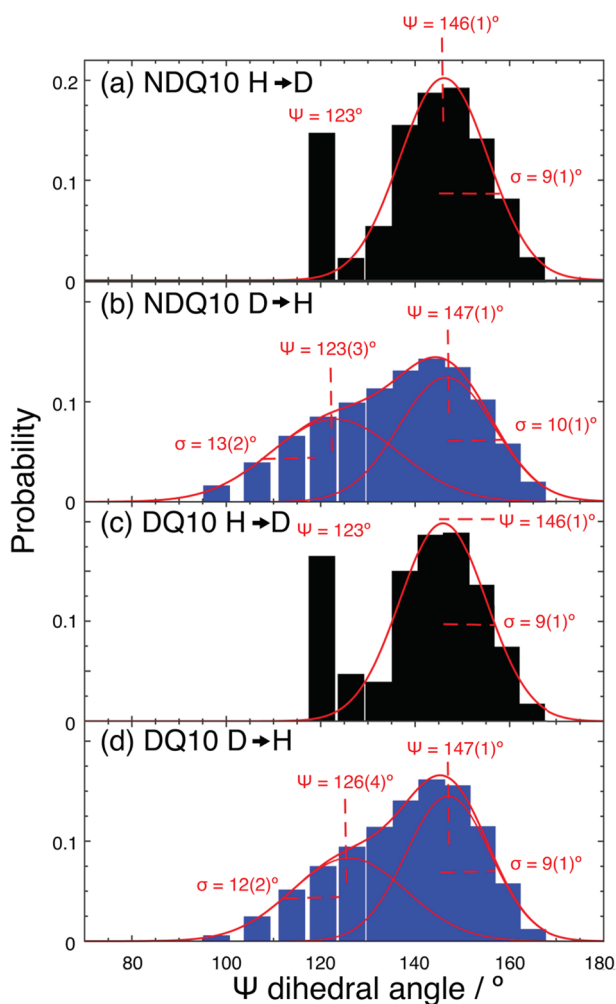


Figure 7. UVRR-determined Ψ angle distributions for NDQ10 and DQ10 fibrils. (a) Distribution corresponding to the NDQ10 fibril Figure 6a HX spectrum. (b) Distribution corresponding to NDQ10 fibril Figure 6b HX spectrum. (c) Distribution corresponding to DQ10 fibril Figure 6c HX spectrum. (d) Distribution corresponding to DQ10 fibril Figure 6d HX spectrum. The distributions were least-squares fit to one or two Gaussians. The peak Ψ angles and distribution standard deviations (σ) are reported, along with their standard errors from the fits (in parentheses).

we employed the methodology of Asher and co-workers^{26,59} (see the Supporting Information for details), which correlates the different frequencies of the AmIII $_3^S$ band envelope to different peptide bond Ψ angles. This enables us to determine a probability distribution of peptide bond Ψ angles from the inhomogeneously broadened AmIII $_3^S$ bandshapes shown in Figure 6. The Ψ distributions shown in black derive from the H \rightarrow D HX-UVRR (Figure 6a,c) AmIII $_3^S$ band profiles, while

those shown in blue are from the D \rightarrow H HX-UVRR (Figure 6b, d) AmIII $_3^S$ band profiles.

As shown in Figure 7, the Ψ angle distributions of NDQ10 and DQ10 are similar, which indicates that the fibril secondary structures are essentially the same. All the distributions are bimodal, showing peaks near $\sim 145^\circ$ and $\sim 125^\circ$. According to Hovmöller et al.'s analysis⁶⁰ of protein data bank crystal structures, Gln residues in antiparallel β -sheet conformations show an average Ψ angle of $\sim 137(15)^\circ$, while those in parallel β -sheet structures show an average Ψ angle of $\sim 129(15)^\circ$. Given these values, we attribute the NDQ10 and DQ10 peaks centered at $\sim 145^\circ$ to fibril peptide bonds that are in antiparallel β -sheet conformations and the peaks at $\sim 125^\circ$ to peptide bonds in parallel β -sheet conformations.

A comparison of the black and blue Ψ angle distributions indicates that there are structural differences between solvent accessible and inaccessible peptide bonds in both NDQ10 and DQ10 fibrils. The blue distributions are much broader than the black distributions, which indicates that the solvent accessible peptide bonds exhibit greater conformational heterogeneity than the solvent inaccessible peptide bonds. Most of this increased structural heterogeneity stems from the peptide bonds in parallel β -sheet conformations. Indeed, the standard deviations (σ) of the antiparallel β -sheet distributions corresponding to solvent accessible and inaccessible peptide bonds are not significantly different. However, the standard deviations of the parallel β -sheet distributions are $\sim 12^\circ$ – 13° for solvent accessible peptide bonds but collapse to a narrower range of Ψ angles for solvent inaccessible peptide bonds.

The Ψ angle distributions shown in Figure 7 indicate that the solvent inaccessible peptide bonds in NDQ10 and DQ10 fibrils preferentially adopt antiparallel over parallel β -sheet conformations. The solvent inaccessible peptide bonds derive primarily from the fibril interiors, where primary fibril nucleation occurs. This suggests that nascent polyQ (proto)fibrils form around antiparallel β -sheet nuclei. In contrast, peptide bonds that are solvent accessible are located predominately on the surface of polyQ aggregates, which is more disordered because peptides can aggregate onto the fibril by forming parallel β -sheet structures, in addition to adding as antiparallel β -sheets.

Developing a Molecular-Level Structural Model. The Figure 7 distributions show that no peptide bonds populate β -turn Ψ angles. Thus, we conclude that the basic structural motifs of NDQ10 and DQ10 fibrils are extended β -strands. To investigate this hypothesis, we utilized atomistic MD to examine Q10 peptides arranged in three different fibril architectures. As shown in Figure 1, these models are composed of eight Q10 peptides arranged into two β -sheet layers. Models *a* and *b* consist of extended β -strands that are arranged into antiparallel and parallel β -sheet architectures, respectively. Model *c* consists of β -hairpins with Type I turn structures that are arranged into an antiparallel β -sheet configuration. Further details regarding the construction of the fibril models for the MD simulations can be found in the Supporting Information.

The Figure 1 simulated fibril models retained structural integrity throughout the energy minimization and equilibration processes of the computations. We utilized an RMSD metric (Figure S2) to monitor the extent of dissociation of the fibril models during the simulation production runs. The RMSD of peptide backbone atoms relative to that of the respective initial, energy-minimized structure was used. An RMSD of 3 Å was used as a dissociation threshold. Based on this criterion, the

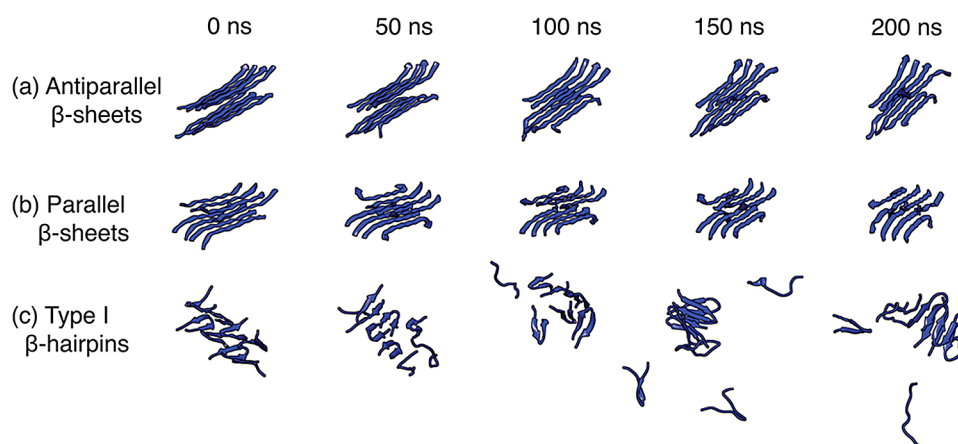


Figure 8. Time evolution of (a) antiparallel β -sheet, (b) parallel β -sheet, and (c) β -hairpin fibril models in MD simulations.

Figure 1c β -hairpin model dissociates at ~ 60 ns into the production simulation, while models *a* and *b* remain intact throughout the full 200 ns simulation (Figure 8).

As shown in Figure 9, we compare the Ramachandran Ψ angle distributions obtained from the production runs of the simulated fibril models to those measured experimentally. The distributions corresponding to models *a* and *b* show large peaks at $\sim 141^\circ$ and $\sim 127^\circ$, respectively, which are very close to the experimentally observed Ψ angle peaks for the antiparallel and parallel β -sheets. In contrast, the model *c* distribution shows very poor agreement with the experimentally determined distributions because the calculated peak Ψ angle distribution is downshifted $\sim 12^\circ$ from the experimentally observed antiparallel β -sheet peak distribution. In addition, the model *c* Ψ angle distribution shows a doublet located at $\sim -19^\circ$ and $\sim -43^\circ$ that is not experimentally observed. This doublet corresponds to Ψ angles that derive from the $i + 1$ and $i + 2$ Type I β -turn residues. The strong agreement between the model *a* and *b* Ψ angle distributions with those measured experimentally supports our conclusion that the basic structural motif of NDQ10 and DQ10 fibrils are stacked β -strands organized into β -sheets.

Our β -strand models for NDQ10 and DQ10 fibrils are consistent with other studies. For example, Schneider et al.⁹ suggested, on the basis of EM and solid-state NMR, that $D_2Q_{15}K_2$ peptides adopt extended β -strands in fibrils. In another study, Thakur and Wetzel⁶¹ probed polyQ fibril structure by replacing Gln-Gln residue pairs with Pro-Gly pairs to increase the formation of β -turn structures. They found that peptides, which had continuous stretches of ~ 9 to 10 Gln residues, mimicked the aggregation behavior and morphologies of unmutated fibrils. They interpret these results to mean that simple polyQ peptides form β -strands that are optimally ~ 9 to 10 Gln residues in length.

Antiparallel β -sheets are Thermodynamically More Favorable than Parallel β -Sheets in PolyQ Fibrils. Numerous studies have shown that the most common structural motif of typical prions and amyloid fibrils is the in-register parallel cross- β structure.^{62–66} For these fibrils, in-register parallel β -sheets appear to maximize hydrophobic and steric zipper interactions.³⁸ Reports of antiparallel β -sheets structures are far less common, although they have been reported for some amyloidogenic peptide microcrystals⁶⁷ and fibrils.⁶⁸ PolyQ fibrils are unique in that most studies^{8,9,12,61} suggest that they predominately form antiparallel β -sheets.

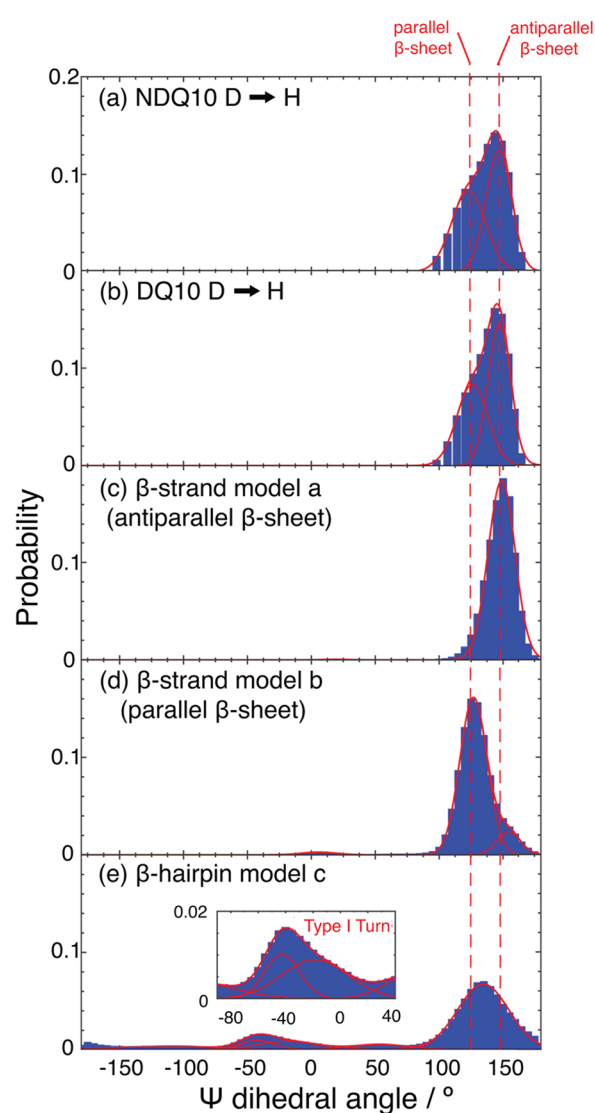


Figure 9. Comparison of Ψ angle distributions from simulations and experiments. The distributions correspond to (a, b) solvent accessible peptide bonds from NDQ10 (Figure 7b) and DQ10 fibrils (Figure 7d), respectively; (c) model *a* in Figure 1; (d) model *b* in Figure 1; and (e) model *c* in Figure 1.

This preference indicates that antiparallel β -sheet structures are more energetically favorable than parallel β -sheets in polyQ fibrils. To examine this possibility, we used the Bennett acceptance ratio method (see the [Supporting Information, Figure S4](#)) to calculate the free energy difference between our simulated parallel and antiparallel β -sheet fibrils. The free energy of our simulated antiparallel β -sheet model system (model *a*) was found to be $160.5(20)$ $\text{kJ}\cdot\text{mol}^{-1}$ (*per fibril system*) lower than the parallel β -sheet model system (model *b*). Because the simulated fibril systems were composed of eight Q10 peptides, this means that the free energy is ~ 1.5 $\text{kJ}\cdot\text{mol}^{-1}$ *per peptide bond* (there are 104 total peptide bonds in each simulated fibril system) lower for the antiparallel β -sheet structure than the parallel β -sheet structure.

The MD simulation results suggest that antiparallel β -sheet formation is favored in polyQ fibrils. This accounts for the greater fraction of antiparallel β -sheets over parallel β -sheets experimentally observed in NDQ10 and DQ10 fibrils. Using the integrated areas of the AmIII^{S} bands in the [Figure 6](#) spectra, we calculate the apparent Gibbs free energy difference between parallel and antiparallel β -sheets to be ~ 6 – 7 $\text{kJ}\cdot\text{mol}^{-1}$ per solvent inaccessible peptide bond and ~ 1 $\text{kJ}\cdot\text{mol}^{-1}$ per solvent accessible peptide bond. We note that the experimentally measured free energy difference of 1 $\text{kJ}\cdot\text{mol}^{-1}$ per solvent accessible peptide bond is very close to the value of ~ 1.5 $\text{kJ}\cdot\text{mol}^{-1}$ per peptide bond calculated from the simulated, well-hydrated fibril models.

We examined electrostatic and hydrogen bonding interactions of models *a* and *b* to understand the origins of the energetic favorability of antiparallel β -sheets over parallel β -sheets. In the case of electrostatics, we find that models *a* and *b* are both stabilized by favorable electrostatic interactions between N-terminal Asp residues and C-terminal Lys residues from opposing β -sheets. However, within a β -sheet, the antiparallel β -sheet model *a* is stabilized by favorable inter-strand electrostatic interactions between oppositely charged terminal residues. In contrast, the parallel β -sheet model *b* is slightly destabilized because of inter-strand electrostatic repulsions of similarly charged terminal residues. The inter-strand repulsion between like-charged terminal residues in model *b* may disrupt nearby peptide backbone hydrogen bonding interactions.

Most of the energetic favorability of the antiparallel β -sheet derives from hydrogen bonding interactions. In our analysis, we considered three different types of peptide–peptide hydrogen bonding: peptide backbone–backbone, side chain–backbone, or side chain–side chain (see [Figure S5](#) and [Table S4](#) in the [Supporting Information](#)). Our analysis indicates that, on average, model *a* forms more peptide–peptide hydrogen bonds than does model *b*. Specifically, model *a* forms significantly more hydrogen bonds between peptide backbone amides than does model *b* ([Figure S5d](#)). In contrast, model *b* forms more side chain–backbone and peptide–water hydrogen bonds than does model *a*, as shown in [Figure S5b,c](#). Thus, it appears that model *a* is stabilized by more peptide–peptide hydrogen bonds and less destabilized because of fewer peptide–water hydrogen bonds. In contrast, model *b* is less energetically favorable because of fewer stabilizing peptide–peptide hydrogen bonds and more destabilizing peptide–water hydrogen bonds. We also note that it is well-known that antiparallel β -sheets are enthalpically more favorable than are parallel β -sheets structures⁶⁹ because of their optimal hydrogen bonding geometries. Our MD results support the hypothesis

that thermodynamics, not kinetics, drive polyQ aggregation into antiparallel β -sheet architectures.

Structure of NDQ10 and DQ10 Gln Side Chains. Determination of Gln Side Chain χ_3 Angle Distributions. We recently discovered³⁰ a vibrational spectral marker band that we call the AmIII^{P} band, which shows a cosinusoidal frequency dependence on the O–C–C–C dihedral angles of Gln and Asn side chains (the χ_3 and χ_2 angles, respectively). The AmIII^{P} vibration is somewhat reminiscent of the AmIII^{S} vibration because it derives from an in-phase combination of C_δ – $\text{N}_{\epsilon 2}$ stretching and $\text{N}_{\epsilon 2}\text{H}_2$ rocking motions (replacing N–H bending in the AmIII^{S}). However, C_β – C_γ stretching also contributes significantly to the AmIII^{P} vibrational potential energy distribution.

The structural sensitivity of the AmIII^{P} band derives mainly from the hyperconjugation of the $\text{C}_\delta=\text{O}_{\epsilon 1}$ π^* and C_β – C_γ σ orbitals.³⁰ When hyperconjugation is strong (e.g., at $\chi_3 \sim \pm 90^\circ$) electron density is transferred from the C_β – C_γ to the $\text{C}_\delta=\text{O}_{\epsilon 1}$ bond. This elongates the C_β – C_γ bond and reduces the C_β – C_γ stretching force constant. As a result, the AmIII^{P} frequency downshifts. In contrast, in the absence of hyperconjugation (e.g., at $\chi_3 \sim 0^\circ$), the C_β – C_γ bond length shortens and the AmIII^{P} frequency upshifts.

To locate the AmIII^{P} bands of NDQ10 and DQ10 fibrils, we curve-resolved the 197–204 nm difference spectra. As shown in [Figure 10](#), the AmIII^{P} band is located between ~ 1050 and 1150 cm^{-1} . Curve-resolving this spectral region for both NDQ10 and DQ10 reveals four underlying bands located at ~ 1060 , ~ 1100 ,

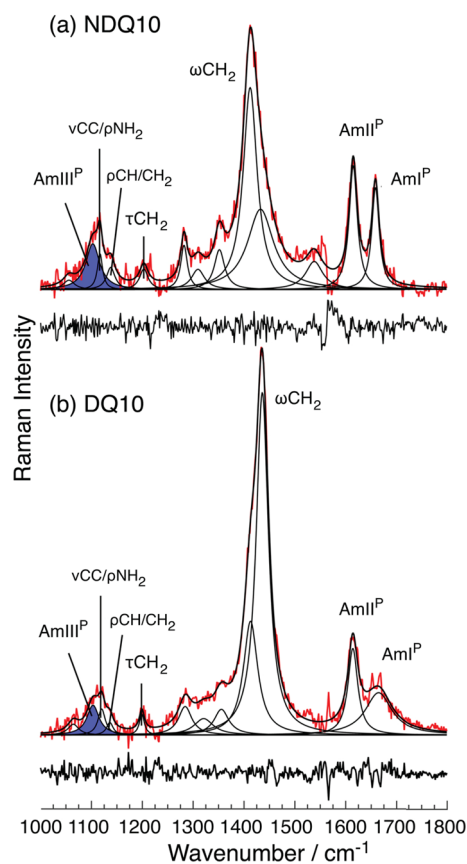


Figure 10. Peak fitting of the 197–204 nm UVRR difference spectra of (a) NDQ10 and (b) DQ10 fibrils. Also shown are the residuals between the fitted and measured spectra. The bands shown in blue are assigned to the AmIII^{P} of the Gln side chains.

~ 1120 , and ~ 1140 cm^{-1} . On the basis of our previous work,³⁰ we assign the 1060, 1120, and 1140 cm^{-1} bands to C–N stretching, C_β – C_γ stretching/ $N_{\epsilon_2}H_2$ rocking, and CH_2 twisting vibrations, respectively. The $AmIII^P$ band is assigned to the ~ 1100 cm^{-1} shoulder feature.³⁰

We utilized the structural sensitivity of the $AmIII^P$ vibration to determine the distributions of χ_3 dihedral angles for the NDQ10 and DQ10 fibrils. The methodology employed to calculate the χ_3 angle distributions is similar to that used to determine the peptide bond Ramachandran Ψ angle distributions (see the Supporting Information for details). As shown in Figure 11a,b, the χ_3 distributions are doubly peaked because the $AmIII^P$ band frequencies give rise to two physically possible χ_3 angle solutions (see the discussion of eq S8 in the Supporting Information). The $AmIII^P$ band of NDQ10 gives rise to distributions of χ_3 angles centered at $\chi_3 \sim -14^\circ$ or 5° . The $AmIII^P$ band of DQ10 gives rise to similar χ_3 angle distributions

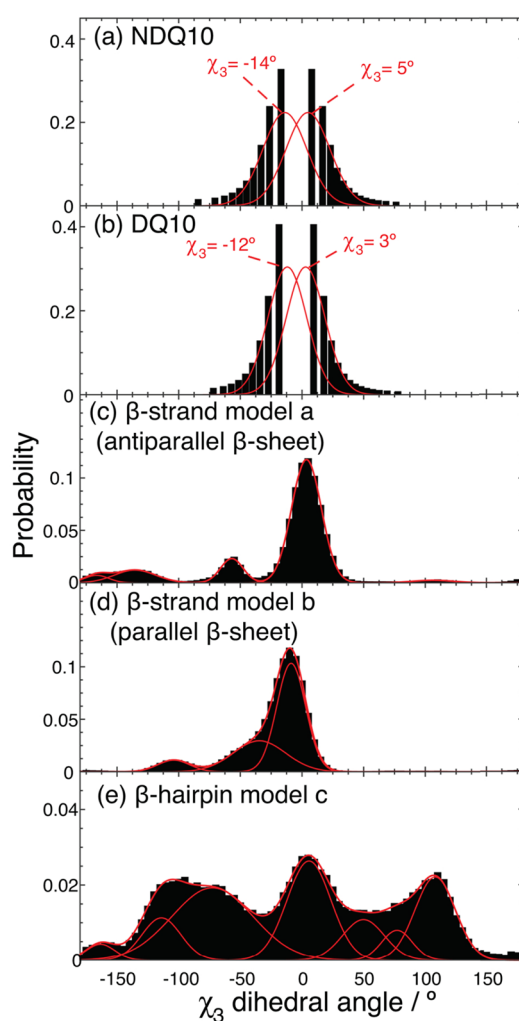


Figure 11. χ_3 dihedral angle distributions of Gln side chains. Distributions obtained experimentally are shown for (a) NDQ10 fibrils and (b) DQ10 fibrils. Distributions obtained from MD simulated structures correspond to (c) model *a* in Figure 1, (d) model *b* in Figure 1, and (e) model *c* in Figure 1. The missing χ_3 angles in panels a and b around the region of $\sim 0^\circ$ are due to the fact that those corresponding $AmIII^P$ frequencies are outside the domain of the semiempirically derived equation³⁰ used to correlate the frequencies of the $AmIII^P$ band envelope to their respective χ_3 angles (see eq S8 in the Supporting Information).

that are centered at $\chi_3 \sim -12^\circ$ or $\sim 3^\circ$. The Gaussian-like distributions of both NDQ10 and DQ10 show standard deviations of $\sim 15^\circ$.

We compared the Figure 11a,b distributions to those calculated from the MD simulated fibril models. The χ_3 dihedral angle distributions corresponding to the simulated fibril models are shown in Figure 11c–e. The antiparallel β -sheet model *a* shows a dominating peak at $\sim 4^\circ$, whereas the parallel β -sheet model *b* shows its largest peak centered at $\sim -10^\circ$. These dihedral angle maxima of models *a* and *b* are very close to the experimentally measured for NDQ10 and DQ10.

Our combined UVRR and validated MD results provide new detailed insights into the structure of the Gln side chains in polyQ fibrils. The experimentally measured χ_3 dihedral angles for both NDQ10 and DQ10 are distributed around $\sim 0^\circ$. As shown by the structures in Figure 12a,b, the model *a* and *b* Gln

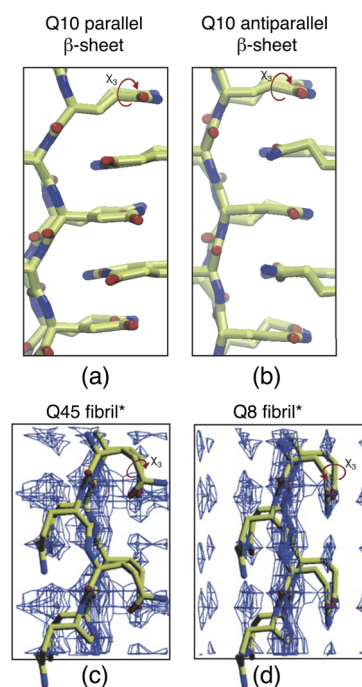


Figure 12. Comparison of side chain geometries from (a, b) our MD simulations and (c, d) Sharma et al.⁸ Panels c and d were adapted with permission from ref 8. Copyright 2005 Wiley.

side chains are approximately planar. This allows Gln side chains from opposing β -sheets to form tightly interdigitated steric zippers, as well as to enable the primary amide groups to both accept and donate hydrogen bonds between neighboring β -strands.

Comparisons of Side Chain Structures with Other Models.

To our knowledge, the structure of Gln side chains in polyQ fibrils has been investigated previously by only the Sikorski⁷ and Kirschner⁸ groups. Both of these studies examined polyQ fibril structure with X-ray diffraction. However, despite obtaining similar diffraction patterns, the Sikorski⁷ and Kirschner⁸ groups proposed different fibril structures based upon modeling the data. For example, the Sikorski⁷ group proposes that Gln side chains show alternating χ_1 ($N-C_\alpha-C_\beta-C_\gamma$) torsion angles along each β -strand of $\sim 69^\circ$ and $\sim -113^\circ$. The Sikorski group's model⁷ is similar to our structure because the Gln side chains are approximately planar; however, their

final model indicates that the χ_3 angle is $\sim 180^\circ$, which is energetically unfavorable and sterically nearly forbidden.³⁰

The Kirschner⁸ group proposed a different structure for Gln side chains in polyQ fibrils. In their study, electron density maps were calculated from their low-resolution powder-like X-ray diffraction patterns by combining the structure factors determined from the experimental reflection intensities and the phase angles from a model that satisfactorily accounted for the observed *d*-spacings. They then modeled the electron densities to generate atomic models for Ac-Q₈-NH₂ and D₂Q₄₅K₂ fibrils. Their modeling of the electron density maps suggests that polyQ fibril Gln side chains adopt unusual bent conformations, as shown in Figure 12c,d. It should be noted that the fibril models reported by the Kirschner⁸ group result in very high *R*-factors (24% for Ac-Q₈-NH₂ and 35% for D₂Q₄₅K₂).

The Kirschner⁸ group's side chain structures are inconsistent with our model. The Kirschner⁸ group structure shows side chain χ_3 angles that approach values of $\sim \pm 90^\circ$, which differs significantly from our experimentally determined values that are close to $\sim 0^\circ$. The fact that we measure χ_3 angles near $\sim 0^\circ$ is important because it means that the Gln side chains are roughly planar, which allows the steric zipper interactions that are believed to stabilize amyloid-like fibrils. It is difficult to envision Gln primary amide stabilizing steric zipper interactions in the Kirschner⁸ group model because their Gln side chain conformations are bent and should not enable tight interdigitation of neighboring β -sheets.

Dependence of Fibril Structure on Deposition of Different NDQ10 and DQ10 Solution Conformations.

The NDQ10 and DQ10 peptides have significantly different solution conformations. The NDQ10 and DQ10 peptide solutions are composed of putative β -hairpin-like and PPII-like conformations, respectively.³⁷ These two solution conformations aggregate into fibrils that are composed of similar, but not identical, β -sheet structures, which have similar planar Gln side chain conformations. The similarity between these fibril structures probably signals that the extended β -strand structure is the most energetically favorable Q10 fibril structure.

However, the subtle differences observed between the NDQ10 and DQ10 fibril structures must result from the variation in the growth mechanisms due to different Q10 solution conformations. A speculative hypothesis is that the increased water content and spacing of the DQ10 fibrils results from the preferential addition of the well-hydrated PPII-like DQ10 peptides that lead to incorporation of water into the hydrophobic interdigitating side chain domains. This gives rise to the longer DQ10 fibril inter- β -sheet spacing compared to NDQ10, as observed in Figure 2. We are presently investigating this possibility.

CONCLUSION

We performed a detailed structural analysis of NDQ10 and DQ10 fibrils using UVRR and MD simulations. On the basis of comparing our UVRR and MD simulation results, we determine that the basic structural element of Q10 fibrils is an extended β -strand. The solvent inaccessible interiors of NDQ10 and DQ10 fibrils are a predominately antiparallel β -sheet structures that are highly ordered and composed of these extended β -strands. However, the water accessible peptide bonds, which are located predominately on the fibril surfaces, show greater conformational heterogeneity and contain significant subpopulations of β -strands that adopt parallel β -sheet architectures.

Our MD simulation results indicate that Q10 antiparallel β -sheets are energetically more favorable than parallel β -sheets. This is an important insight because it may explain why polyQ fibrils, in contrast to most amyloid-like aggregates, preferentially adopt antiparallel β -sheets instead of in-register parallel β -sheets. Our results indicate that the origin of the energetic favorability of Q10 fibril antiparallel β -sheets is mainly due to hydrogen bonding. Antiparallel β -sheets form, on average, more hydrogen bonds between peptide backbone amides than do parallel β -sheets.

This study also provides important new insights into the structure and chemical environment of Gln side chains in polyQ fibrils. In contrast to previous, low-resolution X-ray studies, we show that the Gln side chains in polyQ fibrils adopt conformations that are roughly planar, where the χ_3 dihedral angles are narrowly distributed around 0° . This enables the formation of steric zippers, wherein the side chains of neighboring β -sheets tightly interdigitate.

The UVRR spectra are also highly sensitive to the local hydrogen bonding and dielectric environments of the Gln side chains. For example, a major difference observed between NDQ10 and DQ10 fibrils is a different local dielectric environment of the Gln side chains. The primary amides of both NDQ10 and DQ10 fibrils are strongly hydrogen bonded; however, in DQ10, the side chain methylene groups experience a higher dielectric constant environment. This is likely correlated with the larger DQ10 fibril inter-sheet spacing compared to NDQ10. The larger inter-sheet spacing of DQ10 fibrils presumably results from an increased content of water between β -sheets. The NDQ10 and DQ10 fibrils experience different growth processes due to their different Q10 solution conformations. Deposition of the well-hydrated PPII-like DQ10 peptides results in fibrils with higher water content, with a β -sheet structure showing inter-sheet spacings larger than that which occurs for growth with β -hairpin NDQ10 solution peptides.

Finally, our study demonstrates the utility of synergistically coupling UVRR with MD simulations. Understanding the structure of polyQ and other amyloid-like fibrils remains of great importance because these aggregates are implicated in numerous neurodegenerative diseases. Knowing the fibril structures will provide important insights into the aggregation mechanism(s) of polyQ peptide sequences. However, determining the molecular-level structure of fibrils is challenging because of the insoluble and noncrystalline nature of fibril aggregates. A key advantage of our approach is that UVRR can be utilized to measure the peptide backbone Ψ and the side chain χ_3 dihedral angle distributions. This information can be used to generate hypotheses on the structure of fibrils, which can then be tested *in silico* with MD simulations. Our work combines UVRR and MD into a novel approach for investigating fibrils. Our approach complements existing methods such as solid-state NMR. However, the short experimental UVRR acquisition time frames of our measurements enable the examination of peptide structural changes during fibril aggregation on time scales that are inaccessible to conventional biophysical methods.

NOTE ADDED IN REVISION

While this paper was in review, Hoop et al.⁷⁰ published a study that examined fibrils prepared from the huntingtin exon 1 domain (htt exon 1). Overall, their solid-state NMR (ssNMR) measurements on the polyQ fibril core of htt exon 1 are in

remarkable agreement with our UVRR-based measurements on Q10. Their findings suggest that the polyQ fibril core in htt exon 1 is arranged in β -hairpins that form antiparallel β -sheets. Using sophisticated magic-angle spinning ssNMR techniques, Hoop et al. measured Ramachandran Ψ angles that are very close to our values for antiparallel β -sheets. This is particularly true for their observed “b-type” conformer, where they measure Ψ angles of $\sim 150^\circ$.

Hoop et al. also measured the Gln side chain χ_2 dihedral angles ($C_\alpha-C_\beta-C_\gamma-C_\delta$) to be $\sim 180^\circ$ in htt exon 1 fibrils. Their results lead them to also conclude that the Gln side chains in polyQ fibrils are extended in structure. Although they did not directly measure Gln side chain χ_3 angles, Hoop et al. suggest values of $\pm 150^\circ$, which differ significantly from our experimentally determined values reported here. It is interesting to note that our experimentally validated MD-simulated β -sheet fibril structure (model *a*) shows a mean χ_2 value of $\sim 180^\circ$, which is exactly the angle that Hoop et al. measure. Combining these ssNMR results with our UVRR and MD data leads us to propose that the most likely fibril structures of the Gln side chains will have χ_2 and χ_3 angles of $\sim 180^\circ$ and $\sim 0^\circ$, respectively. We are examining this issue in greater detail.

■ ASSOCIATED CONTENT

Supporting Information

The Supporting Information is available free of charge on the ACS Publications website at DOI: 10.1021/acs.jpcc.5b11380.

Description of UVRR spectral processing and data collection of fibril films; description of density functional theory calculations and band assignments of monodeuterated primary amide group of Gln; and description of Bennett acceptance ratio and RMSD calculations for MD simulations (PDF)

NAMD configuration files and Python scripts used in MD simulations (ZIP)

■ AUTHOR INFORMATION

Corresponding Authors

*E-mail: madura@duq.edu.

*E-mail: asher@pitt.edu.

Notes

The authors declare no competing financial interest.

■ ACKNOWLEDGMENTS

Funding for this work was provided by the University of Pittsburgh (D.P., Z.H., S.A.A.) and partially supported by NIH R01 DA027806 (J.D.M. and R.J.W.). The MD simulation computer time was supported by XSEDE MCB060069, and computer equipment was purchased from NSF funds (CHE-1126465 and P116Z080180). The DFT calculations were supported by the University of Pittsburgh Center for Simulation and Modeling through the supercomputing resources provided. We thank Dr. Sergei V. Bykov, Liqi Feng, Jonathan Weisberg, and Jonathan Wert for useful discussions. We are also grateful to Dr. Steven Geib and Dr. Alexander Makhov for technical assistance with the X-ray diffraction measurements and electron microscopy, respectively.

■ REFERENCES

(1) Orr, H. T.; Zoghbi, H. Y. Trinucleotide Repeat Disorders. *Annu. Rev. Neurosci.* **2007**, *30*, 575–621.

(2) Chen, S.; Berthelie, V.; Yang, W.; Wetzel, R. Polyglutamine Aggregation Behavior In Vitro Supports a Recruitment Mechanism of Cytotoxicity. *J. Mol. Biol.* **2001**, *311*, 173–182.

(3) Mangiarini, L.; Sathasivam, K.; Seller, M.; Cozens, B.; Harper, A.; Hetherington, C.; Lawton, M.; Trotter, Y.; Lehrach, H.; Davies, S. W.; et al. Exon 1 of the HD Gene with an Expanded CAG Repeat is Sufficient to Cause a Progressive Neurological Phenotype in Transgenic Mice. *Cell* **1996**, *87*, 493–506.

(4) Scherzinger, E.; Lurz, R.; Turmaine, M.; Mangiarini, L.; Hollenbach, B.; Hasenbank, R.; Bates, G. P.; Davies, S. W.; Lehrach, H.; Wanker, E. E. Huntingtin-Encoded Polyglutamine Expansions Form Amyloid-like Protein Aggregates In Vitro and In Vivo. *Cell* **1997**, *90*, 549–558.

(5) Perutz, M. F.; Johnson, T.; Suzuki, M.; Finch, J. T. Glutamine Repeats as Polar Zippers: Their Possible Role in Inherited Neurodegenerative Diseases. *Proc. Natl. Acad. Sci. U. S. A.* **1994**, *91*, 5355–5358.

(6) Perutz, M. F.; Finch, J. T.; Berriman, J.; Lesk, A. Amyloid Fibers are Water-Filled Nanotubes. *Proc. Natl. Acad. Sci. U. S. A.* **2002**, *99*, 5591–5595.

(7) Sikorski, P.; Atkins, E. New Model for Crystalline Polyglutamine Assemblies and their Connection with Amyloid Fibrils. *Biomacromolecules* **2005**, *6*, 425–432.

(8) Sharma, D.; Shinchuk, L. M.; Inouye, H.; Wetzel, R.; Kirschner, D. A. Polyglutamine Homopolymers having 8–45 Residues form Slablike β -crystallite Assemblies. *Proteins: Struct., Funct., Genet.* **2005**, *61*, 398–411.

(9) Schneider, R.; Schumacher, M. C.; Mueller, H.; Nand, D.; Klaukien, V.; Heise, H.; Riedel, D.; Wolf, G.; Behrmann, E.; Raunser, S.; et al. Structural Characterization of Polyglutamine Fibrils by Solid-State NMR Spectroscopy. *J. Mol. Biol.* **2011**, *412*, 121–136.

(10) Petkova, A. T.; Ishii, Y.; Balbach, J. J.; Antzutkin, O. N.; Leapman, R. D.; Delaglio, F.; Tycko, R. A Structural Model for Alzheimer's β -amyloid Fibrils Based on Experimental Constraints from Solid State NMR. *Proc. Natl. Acad. Sci. U. S. A.* **2002**, *99*, 16742–16747.

(11) Petkova, A. T.; Yau, W.-M.; Tycko, R. Experimental Constraints on Quaternary Structure in Alzheimer's β -Amyloid Fibrils. *Biochemistry* **2006**, *45*, 498–512.

(12) Sivanandam, V. N.; Jayaraman, M.; Hoop, C. L.; Kodali, R.; Wetzel, R.; van der Wel, P. C. A. The Aggregation-Enhancing Huntingtin N-Terminus Is Helical in Amyloid Fibrils. *J. Am. Chem. Soc.* **2011**, *133*, 4558–4566.

(13) Kar, K.; Hoop, C. L.; Drombosky, K. W.; Baker, M. A.; Kodali, R.; Arduini, I.; van der Wel, P. C.; Horne, W. S.; Wetzel, R. β -Hairpin-Mediated Nucleation of Polyglutamine Amyloid Formation. *J. Mol. Biol.* **2013**, *425*, 1183–1197.

(14) Esposito, L.; Paladino, A.; Pedone, C.; Vitagliano, L. Insights into Structure, Stability, and Toxicity of Monomeric and Aggregated Polyglutamine Models from Molecular Dynamics Simulations. *Biophys. J.* **2008**, *94*, 4031–4040.

(15) Berryman, J. T.; Radford, S. E.; Harris, S. A. Thermodynamic Description of Polymorphism in Q- and N-Rich Peptide Aggregates Revealed by Atomistic Simulation. *Biophys. J.* **2009**, *97*, 1–11.

(16) Miettinen, M. S.; Knecht, V.; Monticelli, L.; Ignatova, Z. Assessing Polyglutamine Conformation in the Nucleating Event by Molecular Dynamics Simulations. *J. Phys. Chem. B* **2012**, *116*, 10259–10265.

(17) Miettinen, M. S.; Monticelli, L.; Nedumpully-Govindan, P.; Knecht, V.; Ignatova, Z. Stable Polyglutamine Dimers Can Contain β -Hairpins with Interdigitated Side Chains-But Not α -Helices, β -Nanotubes, β -Pseudohelices, or Steric Zippers. *Biophys. J.* **2014**, *106*, 1721–1728.

(18) Xu, M.; Shashilov, V. A.; Ermolenkov, V. V.; Fredriksen, L.; Zagorevski, D.; Lednev, I. K. The First step of Hen Egg White Lysozyme Fibrillation, Irreversible Partial Unfolding, is a Two-State Transition. *Protein Sci.* **2007**, *16*, 815–832.

(19) Shashilov, V.; Xu, M.; Ermolenkov, V. V.; Fredriksen, L.; Lednev, I. K. Probing a Fibrillation Nucleus Directly by Deep

Ultraviolet Raman Spectroscopy. *J. Am. Chem. Soc.* **2007**, *129*, 6972–6973.

(20) Xu, M.; Shashilov, V.; Lednev, I. K. Probing the Cross- β Core Structure of Amyloid Fibrils by Hydrogen-Deuterium Exchange Deep Ultraviolet Resonance Raman Spectroscopy. *J. Am. Chem. Soc.* **2007**, *129*, 11002–11003.

(21) Shashilov, V. A.; Lednev, I. K. 2D Correlation Deep UV Resonance Raman Spectroscopy of Early Events of Lysozyme Fibrillation: Kinetic Mechanism and Potential Interpretation Pitfalls. *J. Am. Chem. Soc.* **2008**, *130*, 309–317.

(22) Popova, L. A.; Kodali, R.; Wetzel, R.; Lednev, I. K. Structural Variations in the Cross- β Core of Amyloid β Fibrils Revealed by Deep UV Resonance Raman Spectroscopy. *J. Am. Chem. Soc.* **2010**, *132*, 6324–6328.

(23) Kurouski, D.; Lauro, W.; Lednev, I. K. Amyloid Fibrils are “Alive”: Spontaneous Refolding from One Polymorph to Another. *Chem. Commun.* **2010**, *46*, 4249–4251.

(24) Oladepo, S. A.; Xiong, K.; Hong, Z.; Asher, S. A.; Handen, J.; Lednev, I. K. UV Resonance Raman Investigations of Peptide and Protein Structure and Dynamics. *Chem. Rev.* **2012**, *112*, 2604–2628.

(25) Asher, S. A.; Ianoul, A.; Mix, G.; Boyden, M. N.; Karnoup, A.; Diem, M.; Schweitzer-Stenner, R. Dihedral ψ Angle Dependence of the Amide III Vibration: A Uniquely Sensitive UV Resonance Raman Secondary Structural Probe. *J. Am. Chem. Soc.* **2001**, *123*, 11775–11781.

(26) Mikhonin, A. V.; Bykov, S. V.; Myshakina, N. S.; Asher, S. A. Peptide Secondary Structure Folding Reaction Coordinate: Correlation Between UV Raman Amide III Frequency, Ψ Ramachandran Angle, and Hydrogen Bonding. *J. Phys. Chem. B* **2006**, *110*, 1928–1943.

(27) Miura, T.; Takeuchi, H.; Harada, I. Tryptophan Raman Bands Sensitive to Hydrogen Bonding and Side-Chain Conformation. *J. Raman Spectrosc.* **1989**, *20*, 667–671.

(28) Maruyama, T.; Takeuchi, H. Effects of Hydrogen bonding and Side-Chain Conformation on the Raman bands of Tryptophan-2,4,5,6,7- d_5 . *J. Raman Spectrosc.* **1995**, *26*, 319–324.

(29) Takeuchi, H. Raman Spectral Marker of Tryptophan Conformation: Theoretical Basis and Extension to a Wider Range of Torsional Angle. *J. Mol. Struct.* **2012**, *1023*, 143–148.

(30) Punihaole, D.; Hong, Z.; Jakubek, R. S.; Dahlburg, E. M.; Geib, S.; Asher, S. A. Glutamine and Asparagine Side Chain Hyperconjugation-Induced Structurally Sensitive Vibrations. *J. Phys. Chem. B* **2015**, *119*, 13039–13051.

(31) Chi, Z.; Asher, S. A. UV Raman Determination of the Environment and Solvent Exposure of Tyr and Trp Residues. *J. Phys. Chem. B* **1998**, *102*, 9595–9602.

(32) Hong, Z.; Wert, J.; Asher, S. A. UV Resonance Raman and DFT Studies of Arginine Side Chains in Peptides: Insights into Arginine Hydration. *J. Phys. Chem. B* **2013**, *117*, 7145–7156.

(33) Caswell, D. S.; Spiro, T. G. Ultraviolet Resonance Raman Spectroscopy of Imidazole, Histidine, and $\text{Cu}(\text{Imidazole})_4^{2+}$: Implications for Protein Studies. *J. Am. Chem. Soc.* **1986**, *108*, 6470–6477.

(34) Markham, L. M.; Mayne, L. C.; Hudson, B. S.; Zgierski, M. Z. Resonance Raman Studies of Imidazole, Imidazolium, and their Derivatives: The Effect of Deuterium Substitution. *J. Phys. Chem.* **1993**, *97*, 10319–10325.

(35) Punihaole, D.; Jakubek, R. S.; Dahlburg, E. M.; Hong, Z.; Myshakina, N. S.; Geib, S.; Asher, S. A. UV Resonance Raman Investigation of the Aqueous Solvation Dependence of Primary Amide Vibrations. *J. Phys. Chem. B* **2015**, *119*, 3931–3939.

(36) Buchanan, L. E.; Carr, J. K.; Fluitt, A. M.; Hoganson, A. J.; Moran, S. D.; de Pablo, J. J.; Skinner, J. L.; Zanni, M. T. Structural Motif of Polyglutamine Amyloid Fibrils Discerned with Mixed-Isotope Infrared Spectroscopy. *Proc. Natl. Acad. Sci. U. S. A.* **2014**, *111*, 5796–5801.

(37) Xiong, K.; Punihaole, D.; Asher, S. A. UV Resonance Raman Spectroscopy Monitors Polyglutamine Backbone and Side Chain Hydrogen Bonding and Fibrillization. *Biochemistry* **2012**, *51*, 5822–5830.

(38) Tycko, R.; Wickner, R. B. Molecular Structures of Amyloid and Prion Fibrils: Consensus versus Controversy. *Acc. Chem. Res.* **2013**, *46*, 1487–1496.

(39) Chen, S.; Wetzel, R. Solubilization and Disaggregation of Polyglutamine Peptides. *Protein Sci.* **2001**, *10*, 887–891.

(40) Bykov, S.; Lednev, I.; Ianoul, A.; Mikhonin, A.; Munro, C.; Asher, S. A. Steady-State and Transient Ultraviolet Resonance Raman Spectrometer for the 193–270 nm Spectral Region. *Appl. Spectrosc.* **2005**, *59*, 1541–1552.

(41) Molecular Operating Environment (MOE), 2013.08; Chemical Computing Group Inc.: Montreal, Canada, 2013.

(42) Phillips, J. C.; Braun, R.; Wang, W.; Gumbart, J.; Tajkhorshid, E.; Villa, E.; Chipot, C.; Skeel, R. D.; Kalé, L.; Schulten, K. Scalable Molecular Dynamics with NAMD. *J. Comput. Chem.* **2005**, *26*, 1781–802.

(43) Huang, J.; Mackerell, A. D. CHARMM36 All-Atom Additive Protein Force Field: Validation Based on Comparison to NMR Data. *J. Comput. Chem.* **2013**, *34*, 2135–2145.

(44) Lindorff-Larsen, K.; Piana, S.; Palmo, K.; Maragakis, P.; Klepeis, J. L.; Dror, R. O.; Shaw, D. E. Improved Side-Chain Torsion Potentials for the Amber ff99SB Protein Force Field. *Proteins: Struct., Funct., Genet.* **2010**, *78*, 1950–1958.

(45) Lindorff-Larsen, K.; Maragakis, P.; Piana, S.; Eastwood, M. P.; Dror, R. O.; Shaw, D. E. Systematic Validation of Protein Force Fields Against Experimental Data. *PLoS One* **2012**, *7*, e32131.

(46) Humphrey, W.; Dalke, A.; Schulten, K. VMD: Visual Molecular Dynamics. *J. Mol. Graphics* **1996**, *14*, 33–38.

(47) Jorgensen, W. L.; Chandrasekhar, J.; Madura, J. D.; Impey, R. W.; Klein, M. L. Comparison of Simple Potential Functions for Simulating Liquid Water. *J. Chem. Phys.* **1983**, *79*, 926.

(48) Darden, T.; York, D.; Pedersen, L. Particle Mesh Ewald: An $N \log(N)$ Method for Ewald Sums in Large Systems. *J. Chem. Phys.* **1993**, *98*, 10089–10092.

(49) Shirts, M. R.; Chodera, J. D. Statistically Optimal Analysis of Samples from Multiple Equilibrium States. *J. Chem. Phys.* **2008**, *129*, 1–13.

(50) Chen, S.; Berthelie, V.; Hamilton, J. B.; O’Nuallai, B.; Wetzel, R. Amyloid-like Features of Polyglutamine Aggregates and Their Assembly Kinetics. *Biochemistry* **2002**, *41*, 7391–7399.

(51) Sikorski, P.; Atkins, E. D.; Serpell, L. C. Structure and Texture of Fibrous Crystals Formed by Alzheimer’s $A\beta(11-25)$ Peptide Fragment. *Structure* **2003**, *11*, 915–926.

(52) Dudik, J. M.; Johnson, C. R.; Asher, S. A. UV Resonance Raman Studies of Acetone, Acetamide, and N-Methylacetamide: Models for the Peptide Bond. *J. Phys. Chem.* **1985**, *89*, 3805–3814.

(53) Welch, W. R. W.; Kubelka, J.; Keiderling, T. A. Infrared, Vibrational Circular Dichroism, and Raman Spectral Simulations for β -Sheet Structures with Various Isotopic Labels, Interstrand, and Stacking Arrangements Using Density Functional Theory. *J. Phys. Chem. B* **2013**, *117*, 10343–10358.

(54) Moran, S. D.; Zanni, M. T. How to Get Insight into Amyloid Structure and Formation from Infrared Spectroscopy. *J. Phys. Chem. Lett.* **2014**, *5*, 1984–1993.

(55) Myshakina, N. S.; Ahmed, Z.; Asher, S. A. Dependence of Amide Vibrations on Hydrogen Bonding. *J. Phys. Chem. B* **2008**, *112*, 11873–11877.

(56) Mikhonin, A. V.; Ahmed, Z.; Ianoul, A.; Asher, S. A. Assignments and Conformational Dependencies of the Amide III Peptide Backbone UV Resonance Raman Bands. *J. Phys. Chem. B* **2004**, *108*, 19020–19028.

(57) Uno, T.; Machida, K.; Saito, Y. Infrared Spectra of Partially Deuterated Acetamide. *Bull. Chem. Soc. Jpn.* **1969**, *42*, 897–904.

(58) Uno, T.; Machida, K.; Saito, Y. Out-of-plane Vibrations of Acetamide and Partially N-deuterated Acetamide. *Spectrochim. Acta, Part A* **1971**, *27*, 833–844.

(59) Asher, S. A.; Mikhonin, A. V.; Bykov, S. UV Raman Demonstrates that α -Helical Polyalanine Peptides Melt to Polyproline II Conformations. *J. Am. Chem. Soc.* **2004**, *126*, 8433–8440.

(60) Hovmöller, S.; Zhou, T.; Ohlson, T. Conformations of Amino Acids in Proteins. *Acta Crystallogr., Sect. D: Biol. Crystallogr.* **2002**, *58*, 768–776.

(61) Thakur, A. K.; Wetzel, R. Mutational Analysis of the Structural Organization of Polyglutamine Aggregates. *Proc. Natl. Acad. Sci. U. S. A.* **2002**, *99*, 17014–17019.

(62) Nelson, R.; Sawaya, M. R.; Balbirnie, M.; Madsen, A. O.; Riek, C.; Grothe, R.; Eisenberg, D. Structure of the Cross- β Spine of Amyloid-like Fibrils. *Nature* **2005**, *435*, 773–778.

(63) Paravastu, A. K.; Leapman, R. D.; Yau, W.-M.; Tycko, R. Molecular Structural Basis for Polymorphism in Alzheimer's β -Amyloid Fibrils. *Proc. Natl. Acad. Sci. U. S. A.* **2008**, *105*, 18349–18354.

(64) Wasmer, C.; Lange, A.; Van Melckebeke, H.; Siemer, A. B.; Riek, R.; Meier, B. H. Amyloid Fibrils of the HET-s (218–289) Prion Form a β Solenoid with a Triangular Hydrophobic Core. *Science* **2008**, *319*, 1523–1526.

(65) Marshall, K. E.; Serpell, L. C. Insights into the Structure of Amyloid Fibrils. *Open Biol. J.* **2009**, *2*, 185–192.

(66) Wiltzius, J. J. W.; Landau, M.; Nelson, R.; Sawaya, M. R.; Apostol, M. I.; Goldschmidt, L.; Soriaga, A. B.; Cascio, D.; Rajashankar, K.; Eisenberg, D. Molecular Mechanisms for Protein-Encoded Inheritance. *Nat. Struct. Mol. Biol.* **2009**, *16*, 973–8.

(67) Sawaya, M. R.; Sambashivan, S.; Nelson, R.; Ivanova, M. I.; Sievers, S. A.; Apostol, M. I.; Thompson, M. J.; Balbirnie, M.; Wiltzius, J. J.; McFarlane, H. T.; et al. Atomic Structures of Amyloid Cross- β Spines Reveal Varied Steric Zippers. *Nature* **2007**, *447*, 453–457.

(68) Tycko, R.; Sciarretta, K. L.; Orgel, J. P. R. O.; Meredith, S. C. Evidence for Novel β -Sheet Structures in Iowa Mutant β -Amyloid Fibrils. *Biochemistry* **2009**, *48*, 6072–6084.

(69) Perczel, A.; Gáspári, Z.; Csizmadia, I. G. Structure and Stability of β -Pleated Sheets. *J. Comput. Chem.* **2005**, *26*, 1155–1168.

(70) Hoop, C. L.; Lin, H.-K.; Kar, K.; Magyarfalvi, G.; Lamley, J.; Boatz, J.; Mandal, A.; Lewandowski, W. R., Jr.; Wetzel, R.; van der Wel, P. C. A. Huntingtin Exon 1 Fibrils Feature an Interdigitated β -hairpin-based Polyglutamine Core. *Proc. Natl. Acad. Sci. U. S. A.* **2016**, *113*, 1546–1551.